Large area CMOS active pixel sensor x-ray imager for digital breast tomosynthesis: Analysis, modeling, and characterization

Chumin Zhao and Jerzy Kanicki[a)]
Solid-State Electronics Laboratory, Department of Electrical Engineering and Computer Science, University of Michigan, Ann Arbor, Michigan 48109

Anastasios C. Konstantinidis
Department of Medical Physics and Biomedical Engineering, University College London, London WC1E 6BT, United Kingdom and Diagnostic Radiology and Radiation Protection, Christie Medical Physics and Engineering, The Christie NHS Foundation Trust, Manchester M20 4BX, United Kingdom

Tushita Patel
Department of Physics, University of Virginia, Charlottesville, Virginia 22908

(Received 19 December 2014; revised 13 August 2015; accepted for publication 22 September 2015; published 8 October 2015)

Purpose: Large area x-ray imagers based on complementary metal-oxide-semiconductor (CMOS) active pixel sensor (APS) technology have been proposed for various medical imaging applications including digital breast tomosynthesis (DBT). The low electronic noise (50–300 e^-) of CMOS APS x-ray imagers provides a possible route to shrink the pixel pitch to smaller than 75 μm for microcalcification detection and possible reduction of the DBT mean glandular dose (MGD).
Methods: In this study, imaging performance of a large area (29×23 cm^2) CMOS APS x-ray imager [Dexela 2923 MAM (PerkinElmer, London)] with a pixel pitch of 75 μm was characterized and modeled. The authors developed a cascaded system model for CMOS APS x-ray imagers using both a broadband x-ray radiation and monochromatic synchrotron radiation. The experimental data including modulation transfer function, noise power spectrum, and detective quantum efficiency (DQE) were theoretically described using the proposed cascaded system model with satisfactory consistency to experimental results. Both high full well and low full well (LFW) modes of the Dexela 2923 MAM CMOS APS x-ray imager were characterized and modeled. The cascaded system analysis results were further used to extract the contrast-to-noise ratio (CNR) for microcalcifications with sizes of 165–400 μm at various MGDs. The impact of electronic noise on CNR was also evaluated.
Results: The LFW mode shows better DQE at low air kerma ($K_a < 10$ μGy) and should be used for DBT. At current DBT applications, air kerma ($K_a \sim 10$ μGy, broadband radiation of 28 kVp), DQE of more than 0.7 and ~0.3 was achieved using the LFW mode at spatial frequency of 0.5 line pairs per millimeter (lp/mm) and Nyquist frequency ~6.7 lp/mm, respectively. It is shown that microcalcifications of 165–400 μm in size can be resolved using a MGD range of 0.3–1 mGy, respectively. In comparison to a General Electric GEN2 prototype DBT system (at MGD of 2.5 mGy), an increased CNR (by ~10) for microcalcifications was observed using the Dexela 2923 MAM CMOS APS x-ray imager at a lower MGD (2.0 mGy).
Conclusions: The Dexela 2923 MAM CMOS APS x-ray imager is capable to achieve a high imaging performance at spatial frequencies up to 6.7 lp/mm. Microcalcifications of 165 μm are distinguishable based on reported data and their modeling results due to the small pixel pitch of 75 μm. At the same time, potential dose reduction is expected using the studied CMOS APS x-ray imager.
© *2015 American Association of Physicists in Medicine.* [http://dx.doi.org/10.1118/1.4932368]

Key words: CMOS x-ray detector, active pixel sensor, digital breast tomosynthesis, cascaded system analysis, microcalcifications

1. INTRODUCTION

Current clinical x-ray imagers for digital breast tomosynthesis (DBT) are dominated by the hydrogenated amorphous silicon (a-Si:H) thin-film transistor (TFT) passive pixel sensor (PPS) technology.[1,2] Both indirect a-Si:H p–i–n photodiode (PD) in combination with a thallium-activated structured cesium iodide (CsI:Tl) scintillator and a direct amorphous selenium (a-Se) photoconductor are used for DBT products.[3–5] Even though the PPS can achieve a compact pixel layout and large area manufacturing, it suffers from high electronic noise of greater than 1000 electrons (e^-).[6] In addition, the rapid reduction of fill factor for smaller pixel sizes represents a significant limitation on the pixel resolution with PPS x-ray imagers. The high electronic noise (1000–2000 e^-) and limited fill factor (<0.7) restrict the DBT pixel pitch to values ranging from 85 to 140 μm (after pixel binning),[2] and the mean glandular dose (MGD) to around 1.3 mGy for an average breast with 5 cm thickness and 50% glandular fraction.[7] A large pixel pitch will result in loses of image information such as small

size microcalcifications and fine details contained in the high spatial frequency region beyond 5 line pairs per millimeter (lp/mm).

Digital x-ray imagers based on complementary metal-oxide-semiconductor (CMOS) active pixel sensor (APS) technology have been developed in the past two decades.[8,9] The CMOS APS sensors differ from the conventional PPS sensors by adding an amplifier to each pixel to increase the signal-to-noise ratio (SNR).[10] In contrast to the single-transistor PPS pixel, the simplest CMOS APS pixel circuit consists of a crystalline silicon (c-Si) photodiode and three field-effect transistors.[10,11] A scintillator such as CsI:Tl needs to be coupled with the CMOS APS sensors to convert the x-rays to optical photons that are detected indirectly by the photodiode.[12] The advantages of CMOS APS technology over PPS are (i) small pixel pitch (25–100 μm), (ii) low electronic noise (50–300 e^-), (iii) fast frame rate [up to 30 frames per second (fps)], and (iv) full circuit integration.[13,14] In the past few years, wafer scale (~10 cm) CMOS APS arrays have been developed for medical imaging applications.[14–17] A number of wafer scale CMOS APS arrays can be tiled together to achieve a large detector area with the dimension of $\sim 20 \times 30$ cm^2 that is suitable for digital mammography and DBT.[18,19] More specifically, the image quality metrics such as modulation transfer function (MTF), noise power spectrum (NPS), and detective quantum efficiency (DQE) of a 29×23 cm^2 large area CMOS APS x-ray imager [Dexela 2923 MAM (PerkinElmer, London)] with a ~75 μm pixel pitch have been measured by various groups for both digital mammography and DBT.[18–21] The pixel size is capable of achieving a high Nyquist frequency (f_{Nyq}) of ~6.7 lp/mm for improved image quality. DQE of greater than 0.6 was achieved under DBT exposure conditions.[18] Naday *et al.*[20] and Park *et al.*[22] also investigated the reconstructed image quality using the Dexela x-ray imager. It has been shown that microcalcifications with size of 165 μm are distinguishable using CMOS APS technology.[22]

The cascaded system analysis provides another approach to theoretically investigate the x-ray imager performance.[23–28] Detector key parameters for a series of gain and spreading stages must be extracted to calculate the image quality metrics such as MTF, NPS, and DQE. Three dimensional (3D) cascaded system model can be used to investigate the noise aliasing effect.[29] The cascaded system analysis that is commonly used for a-Si:H based PPS x-ray imagers has not been applied to CMOS APS x-ray imagers.

In this work, the imaging performance of the Dexela 2923 MAM CMOS x-ray imager was analyzed, characterized, and modeled for DBT application. More specifically, a reliable model based on cascaded system analysis was developed for a CMOS APS x-ray imager. This analysis was applied to simulate the experimental data of MTF, NPS, and DQE parameters for both broadband[18] and monochromatic synchrotron radiations.[19]

Clinically, radiologists search for clusters of microcalcifications with dimensions ranging from 100 to 500 μm as important early indicators of breast cancers.[30] Detection of microcalcifications in small sizes below 200 μm is critical but also challenging because of the limited pixel resolution of current PPS x-ray imagers. The novelty of this work is to numerically calculate the contrast-to-noise ratio (CNR) for microcalcifications with various sizes (165–400 μm) using the cascaded system modeling results based on the high resolution CMOS APS x-ray imager. At the same time, we analyzed the impact of electronic noise on image quality of microcalcifications as defined by CNR at various calculated MGDs.

2. MATERIALS AND METHODS

2.A. Dexela 2923 MAM CMOS APS x-ray imager

The Dexela 2923 MAM CMOS APS x-ray imager used in this work is based on a 3-transistor (3-T) CMOS APS technology. Detailed technical description of this x-ray imager is not provided in the open literature. Figure 1 shows a typical example of the circuit schematic (a) and driving scheme (b) of the 3-T CMOS APS pixel circuit and the cross-sectional view of a c-Si photodiode. The cross section of the reset transistor T_{RST} is also shown. T_{SF}, T_{SEL}, and T_{BIAS} represent source follower, row select transistors for the APS pixel, and bias transistor in the column line, respectively. Details of the 3-T CMOS APS operation principle and driving scheme are described in Appendix A.

The Dexela 2923 MAM x-ray imager offers an option to switch between high full well (HFW) and low full well

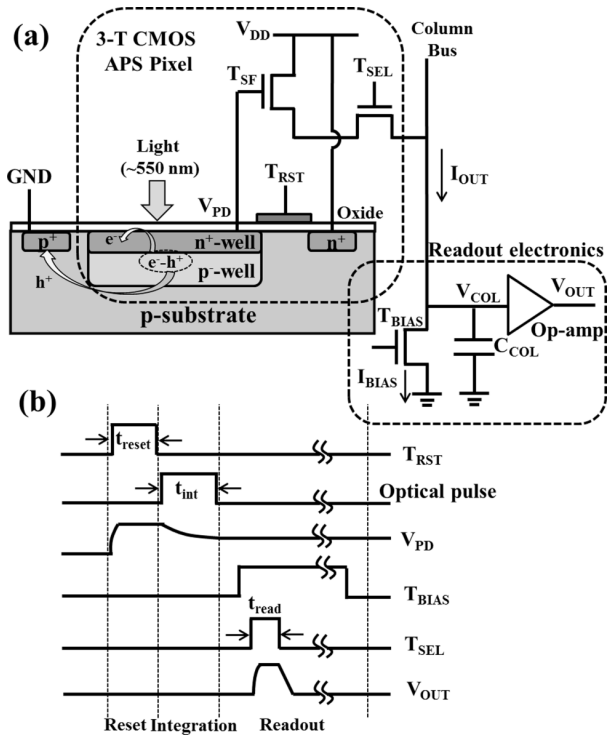

FIG. 1. (a) Circuit schematic of 3-T CMOS APS pixel and readout electronics with cross-sectional view of the c-Si photodiode and T_{RST} shown. T_{RST}, T_{SF}, and T_{SEL} stand for the reset transistor, source follower, and row select transistor for the pixel; T_{BIAS} is the column bias transistor and C_{COL} is the storage capacitor for the column bus line. (b) Driving scheme of the 3-T CMOS APS x-ray imager based on n-MOS technology.

(LFW) modes.[16,18,19] The full well capacity is defined as the maximum number of electrons that can be stored on the sensing node (V_{PD} in Fig. 1). The HFW mode is designed to achieve high full well capacity ($N_{HFW} \sim 1.6\times10^6$ e$^-$) and high dynamic range (~73 dB) but at the expense of higher electronic noise (~360 e$^-$).[16,19] In comparison, the LFW mode has a relatively lower full well capacity ($N_{LFW} \sim 0.5\times10^6$ e$^-$), smaller dynamic range (69 dB), and lower electronic noise (165 e$^-$).[16,19] The LFW is more sensitive to small signal, but is limited in dynamic range. In general, switching between HFW and LFW modes can be achieved by adding an additional input storage capacitor (C_S) to the photodiode capacitance (C_{PD}). If we consider C_{PD} is approximately constant under various reverse bias, the full well capacity can be described as $N_{HFW} = (C_S + C_{PD})\times V_{DD}/q$ and $N_{LFW} = C_{PD}\times V_{DD}/q$ for HFW and LFW modes, respectively. Assuming that V_{DD} is in the range of 1–3 V, the corresponding total input capacitance for HFW ($C_S + C_{PD}$) and LFW (C_{PD}) modes of Dexela 2923 MAM CMOS APS x-ray imager can be calculated to be 85–255 fF and 27–81 fF, respectively. For the LFW mode, the small C_{PD} will result in a larger conversion gain; reported values in the literatures are 8.4×10^{-3} and 0.026 digital numbers per electron (DN/e$^-$) for HFW and LFW modes, respectively.[16]

2.B. Detector x-ray imaging performance evaluation

The imaging performance of CMOS APS x-ray imager was evaluated by measuring the MTF, NPS, and DQE parameters for both broadband[18] and monochromatic synchrotron radiations.[19] Figure 2 shows the schematics of broadband[18] and a monochromatic synchrotron radiations.[19] In both cases, the IEC standard recommendations were used for measurements of MTF, NPS, and DQE parameters.[31]

The x-ray source for the broadband radiation is a tungsten anode (W) with a beryllium (Be) exit window filtration of 0.76 mm thickness and an external rhodium filter of 0.05 mm thickness.[18] An additional 1.4 mm aluminum (Al) filtration was added to match the half value layer (HVL) of 0.75 mm Al specified in IEC protocol 62220-1-2 for mammography.[31] The x-ray tube voltage was set at 28 kVp.

The x-ray beams of monochromatic synchrotron radiation were generated from one of the bending magnets of the storage ring (Fig. 2). The energy was selected using a double-crystal Si monochromator.[19]

The tilted edge technique described by Buhr *et al.* and Samei *et al.* was used to measure the MTF.[32,33] The details on MTF measurement were discussed in previous work.[16,18,19] Briefly, an opaque object such as W foil with a sharp edge was placed on the detector with a small tilted angle of 1.5°–3° referring to the pixel rows and columns. The edge spread function (ESF) of several consecutive rows or columns was obtained by reading the output signal of corresponding pixels. The ESF curves were then shifted and combined to the average oversampled ESF curve to reduce the statistical noise. Then, the oversampled line spread function (LSF) curve was derived by differentiating the oversampled ESF curve. The final MTF(u) as a function of spatial frequency u was calculated by normalizing the Fourier transform (FT) of oversampled LSF.[19] Suppose x is in the horizontal direction, corresponding MTF(v) in the vertical direction can be obtained by repeating the procedure in the y direction.

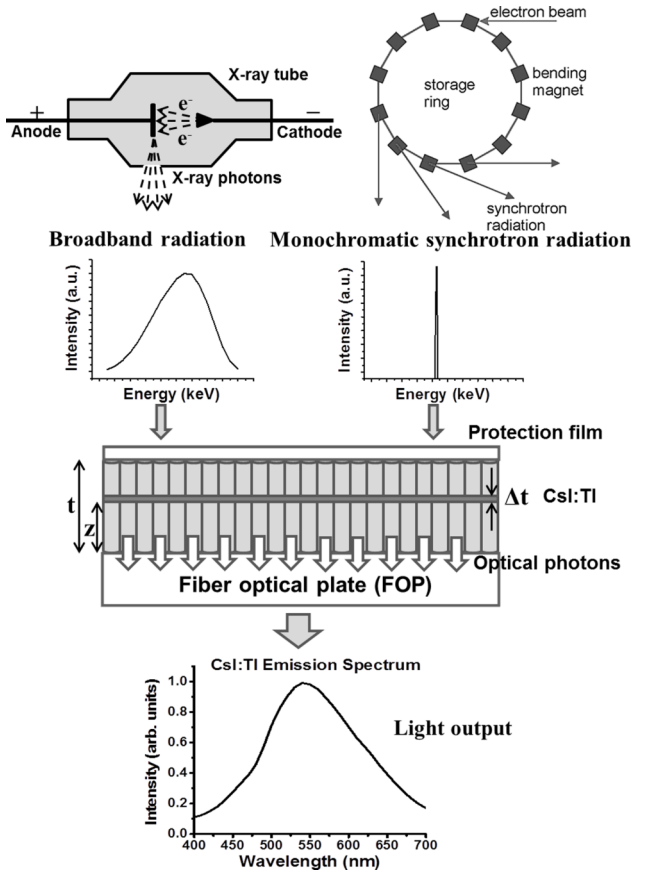

FIG. 2. Schematic of the x-ray generation and cross-sectional view of the scintillator, protection film, and fiber optic plate (FOP) combination. The broadband and monochromatic synchrotron radiation spectra as a function of energy and the light output as a function of wavelength are shown.

To calculate the NPS, a large area flat field image for region of interest (ROI) of 2380 × 3664 pixels for broadband x-ray radiation and 2350 × 2350 pixels for monochromatic synchrotron radiation was obtained.[18,19] The ROI was separated into M subROIs of 256 × 256 pixels half-overlapping with each other. The NPS as a function of spatial frequency can be extracted from the FT of flat field image $I(x_i,y_i)$ subtracted by a second order polynomial fit $S(x_i,y_i)$ to remove low frequency (background) trends arising for the x-ray field's nonuniformity (e.g., heel effect),[19]

$$\mathrm{NPS}(u,v) = \frac{\Delta x\cdot\Delta y}{M\cdot N_x\cdot N_y}\sum_{i=1}^{M}\left|\mathrm{FT}\{I(x_i,y_i) - S(x_i,y_i)\}\right|, \quad (1)$$

where Δx and Δy are the pixel pitches in x and y directions, N_x and N_y represent the subROI size (256 × 256), M is the total number of subROIs, $I(x_i,y_i)$ is the flat field image for subROI i as a function of x and y, and $S(x_i,y_i)$ is a second order polynomial fit according to the IEC standard.[31] The normalized NPS (NNPS) can be calculated by dividing NPS by the square of mean pixel output signal (d in DN).[19] Finally,

the DQE can be extracted from measured MTF and NNPS parameters by the following expression:

$$\mathrm{DQE}(u,v) = \frac{d^2\mathrm{MTF}^2(u,v)}{\overline{q_0}\mathrm{NPS}(u,v)} = \frac{\mathrm{MTF}^2(u,v)}{\overline{q_0}\mathrm{NNPS}(u,v)}, \quad (2)$$

where d is the mean pixel output signal in DN and $\overline{q_0}$ is the mean x-ray fluence in x-rays/mm^2.

2.C. Cascaded system analysis for CMOS APS x-ray imagers

To investigate and predict the imaging performance of CMOS APS x-ray imagers under various exposure conditions, cascaded system analysis is an effective tool. It can be used to simulate both signal and noise transfers between a series of gain and blurring stages. The cascaded system of CMOS APS x-ray imager can be described by the following eight stages.[23,24]

Stage 0: Incident x-ray quanta. The input x-ray signal (mean x-ray fluence, $\overline{q_0}$) is determined by the number of incident x-ray photons for an x-ray spectrum per unit area (in x-rays/mm^2) of the imager. $\overline{q_0}$ is proportional to the input air kerma (K_a) at detector surface. The mean x-ray fluence per input air kerma, $\overline{q_0}/K_a$ (in x-rays/mm^2 per μGy), can be obtained using the incident x-ray spectrum ($\Phi(E)$) and the mass energy-absorption coefficient of dry air $(\mu_{\mathrm{en}}/\rho)_{\mathrm{air}}$ in cm^2/g as a function of x-ray energy E.[34]

Stage 1: X-ray absorption by scintillator (gain stage). The probability that an incident x-ray photon with energy E being absorbed by or interacted with the scintillator is described by the quantum detection efficiency (QDE). The QDE as a function of x-ray photon energy is given by[19,23,35]

$$\mathrm{QDE}(E) = 1 - \exp\left[-\left(\frac{\mu}{\rho}(E)\right)\rho_S\right], \quad (3)$$

where μ/ρ is the energy-dependent mass attenuation coefficient of scintillator such as CsI:Tl and ρ_S represents the surface density in the unit g/cm^2. For an incident x-ray spectrum with the maximum x-ray energy $E_{\max}$, the scintillator mean quantum efficiency ($\bar{g}_1$), describing the mean absorption of the x-ray spectrum, is given by[23,24,34]

$$\overline{g_1} = \frac{\int_0^{E_{\max}} \Phi(E)\cdot\mathrm{QDE}(E)\cdot T_0(E)\,\mathrm{d}E}{\int_0^{E_{\max}} \Phi(E)\,\mathrm{d}E}, \quad (4)$$

where $T_0(E)$ represents the transmittance of the scintillator top protection film, such as Al. $T_0(E)$ is approximately 0.95 assuming that a thin protection film of Al (<100 μm) is used.[36] $\overline{g_1}$ reflects the mean number of absorbed x-rays per incident x-ray quanta. In general, QDE is scintillator thickness dependent, i.e., a thicker CsI:Tl layer produces a higher QDE.[37] However, at the same time, the long optical path in the scintillating material degrades the DQE at high spatial frequencies due to the light scattering effect. In this work, CsI:Tl scintillator thicknesses of 150 μm (broadband x-ray radiation, 28 kVp)[18] and 200 μm (monochromatic synchrotron radiation, 17 keV)[19] were used.

Stage 2: Optical photon generation and emission by scintillator (gain stage). The absorbed x-rays are converted into optical photons in the scintillator. The conversion process can be divided into three consecutive stages: (a) the excitation of electrons in the inner shell, and relaxation and creation of a large number of electron–hole (e–h) pairs through an avalanche process; (b) carrier migration and further relaxation leading to formation of excitons, having an energy smaller than the bandgap; and (c) e–h recombination and light emission (photoluminescence).[38,39] In general, to create an e–h pairs, an average energy (E_{eh}) greater than compound's bandgap (E_g) is required.[38]

The number of optical photons generated inside the scintillator by an absorbed x-ray photon with energy E is given by[38,39]

$$N_{\mathrm{ph}}(E) = N_{\mathrm{eh}}(E)\cdot S\cdot Q = \frac{E}{E_{\mathrm{eh}}}\cdot S\cdot Q, \quad (5)$$

where $N_{\mathrm{eh}}(E)$ is the number of e–h pairs generated by a single x-ray photon with energy E, S is the transfer efficiency of the e–h pair energy to the luminescent center inside the bandgap, Q is the luminescence quantum efficiency, and E_{eh} is the average energy required to create one e–h pair. The optical yield (in photons/keV), the number of optical photons generated by a single x-ray photon per unit x-ray energy, is given by

$$\eta_{\mathrm{opt}} = \frac{N_{\mathrm{ph}}(E)}{E} = \frac{1}{E_{\mathrm{eh}}}\cdot S\cdot Q. \quad (6)$$

For CsI:Tl, E_{eh} is around $2.5E_g$ and E_g is 6.4 eV.[40] S and Q are dependent on the material manufacturing technology. Assuming S and Q equal to 1 (ideal case), the calculated maximum η_{opt} of CsI:Tl is 62 photons/keV, which is within the range of reported experimental values ranging from 52 to 66 photons/keV.[39,41]

In the cascaded system simulation described in this paper, η_{opt} of 55 photon/keV was used to achieve good fit to experimental data.

After the optical photon generation, the probability of emitted optical photons escaping from the scintillator (η_{esc}) depends on the vertical distance (z) from the bottom interface.[42] The light output (number of optical quanta emitted) per absorbed x-ray photon of energy E at a distance z from the scintillator bottom interface is given by[23]

$$g_2(E,z) = \eta_{\mathrm{opt}}\cdot\eta_{\mathrm{esc}}(z)\cdot E. \quad (7)$$

It should be noticed that no K-fluorescence x-rays were generated, since the maximum x-ray energy used (28 keV) was below the K-absorption edges of CsI:Tl scintillator [i.e., 33.2 keV for iodine (I) and 36 keV for cesium (Cs)].

The mean quantum gain ($\bar{g}_2$) of scintillator with a thickness t can be obtained by integrating the light output at various E and z,[23]

$$\overline{g_2} = \frac{\int_0^{E_{\max}} \Phi(E)\left[\int_{z=t}^{0} e^{-\mu(E)(t-z)}\left(1-e^{-\mu(E)\Delta t}\right) g_2(E,z)\,\mathrm{d}z\right]\mathrm{d}E}{\int_0^{E_{\max}} \Phi(E) g_1(E)\,\mathrm{d}E}, \quad (8)$$

where $g_1(E) = \mathrm{QDE}(E) \times T_0(E)$, and $e^{-\mu(t-z)}$ and $(1-e^{-\mu\Delta t})$ represent the probabilities of x-rays passing through the distance $(t-z)$ and absorbed by a thin layer of thickness Δt (Fig. 2), respectively. The integral can be calculated by summation over E and z. The $\overline{g}_2$ describes the mean number of optical photons escaped from the scintillator over the entire optical spectrum per absorbed x-ray photon.

The scintillator Poisson excess ε_{g_2} is given by[25]

$$\varepsilon_{g_2} = \overline{g_2}\left(\frac{1}{I_{\mathrm{Swank}}} - 1\right) - 1, \tag{9}$$

where I_{Swank} is the Swank factor describing the noise associated with the x-ray conversion process in scintillator.[25,27,37]

Stage 3: Light scattering by scintillator (stochastic blurring stage). This stage describes the scattering effect of the scintillator. The second order polynomial fit for $T_3(u,v)$ generally used to describe scintillator MTF[24] ($T_3(u,v)$) does not provide good fitting for Dexela 2923 MAM CMOS APS x-ray imager. The deviation can originate from the additional FOP blurring effect, which was not included in the current model. To provide a better fitting to experimental data, we used an exponential decay function to fit the measured system one dimensional (1D) MTF,

$$\mathrm{MTF}(u) = A \times \exp(-u/B) + C, \tag{10}$$

where A, B, and C are fitting parameters as shown in Table I. Then, $T_3(u,v)$ was calculated by dividing the fitted system MTF by the transfer function of the pixel aperture $T_6(u,v)$ as described in stage 6. As the result, the calculated $T_3(u,v)$ can be considered as an integrated stage for both scintillator and FOP blurring. It should be noted that this exponential decay function is used to analyze data up to the Nyquist frequency.

Stage 4: Optical coupling of FOP (gain stage). A FOP attached to the scintillator is widely used in CMOS x-ray imagers.[19,43] The optical photons escaping from the scintillator are coupled to the photodiode through the FOP. In addition, the FOP operates as an x-ray blocking material to prolong the lifetime of the x-ray imager. The optical coupling efficiency, which determines the fraction of optical photons coupled and transmitted by the FOP, is given by[44]

$$\overline{g_4} = \mathrm{NA}^2 \cdot T_F \cdot (1 - L_R) \cdot F_C, \tag{11}$$

where NA (~1) is the numerical aperture of a fiber optic, T_F (~0.8) is the transmission of the fiber optic core, L_R (~10%) is the optical loss at the surface due to Fresnel reflection, and F_C (0.75–0.85) is fill factor of the fiber optic core.[44] The typical thickness of FOP is ~3 mm. The calculated FOP optical coupling efficiency is ranging from around 0.54 to 0.61.

In this work, $\overline{g_4}$ of 0.55 was used. Note that the FOP blurring was not investigated as an individual stage. However, the $T_3(u,v)$ extracted in stage 3 can be considered as an integrated stage for both scintillator and FOP blurring.

Stage 5: Optical photon absorption and electron generation by photodiode (gain stage). The optical photons transmitted through FOP are coupled to the c-Si CMOS APS imager to create e–h pairs (electronic signal) inside the photodiode. (Details of this process are described in Appendix A.) The captured electrons per incident photon can be described by the photodiode external quantum efficiency (EQE). The mean number carriers collected per incident optical photon are $\overline{g_5}$ = EQE.

In the current study, we used EQE of ~0.6.

The electronic signal (in e^-) is then amplified by APS pixel circuitry and finally converted to output voltage (or DN). (For more details, see Appendix A.)

Stage 6: Pixel presampling (deterministic blurring stage). The transfer function due to pixel aperture (photodiode active area) $T_6(u,v)$ in the spatial frequency (u,v) domain is given by

$$T_6(u,v) = \left|\mathrm{sinc}(\pi a_{\mathrm{pd}} u) \cdot \mathrm{sinc}(\pi a_{\mathrm{pd}} v)\right|, \tag{12}$$

where a_{pd} is the effective photodiode pitch. Given the pixel pitch (a_{pix}) of the detector (75 μm), a_{pd} is calculated by a_{pd}^2

TABLE I. Parameters used in the cascaded system model.

Parameters	Value (broadband, 28 kVp)	Value (monochromatic, 17 keV)	Description
$\overline{q_0}/K_a$	5975 (x-rays/mm^2)/μGy	4083 (x-rays/mm^2)/μGy	Mean x-ray fluence/air kerma
$\bar{g}_1$	0.72	0.89	Mean x-ray absorption
$\bar{g}_2$	612	543	Scintillator mean quantum gain
I_{Swank}	0.91	0.90	Swank factor
ε_{g_2}	59.5	59.3	Scintillator Poisson excess
A	0.97	1.05	Fitting parameter A for 1D MTF
B	3.10	4.50	Fitting parameter B for 1D MTF
C	0.03	−0.05	Fitting parameter C for 1D MTF
$\bar{g}_4$	0.55	0.55	FOP optical coupling efficiency
$\bar{g}_5$	0.60	0.60	Photodiode EQE
a_{pix}	75 μm	75 μm	Pixel pitch
a_{pd}	68.7 μm	68.7 μm	Effective photodiode pitch
FF	0.84	0.84	Pixel fill factor
σ_{add}	360 e^- (HFW) 165 e^- (LFW)	360 e^- (HFW) 165 e^- (LFW)	Additive electronic noise

$= a_{pix}^2 \times FF$, where FF (0.84) is the pixel fill factor [ratio of photodiode active area (a_{pd}^2) to the total pixel area (a_{pix}^2)]. Here, we assume that the photodiode active area is square.

Stage 7: NPS aliasing. The maximum spatial resolution is limited to $1/(2a_{pix})$ because of the aliasing effect, which is included in this stage. The NPS aliasing is included in this stage. The term III_7 is a Fourier domain comb function as a sum of equally spaced delta functions indicating the aliasing effect of NPS.[27,28]

Stage 8: Additive CMOS APS electronic noise. The additive electronic noise (σ_{add}) for HFW and LFW modes was extracted in previous works from the photon transfer curve (PTC) analysis method.[16,19] In this work, σ_{add} of 360 and 165 e^- for HFW and LFW modes of the Dexela 2923 MAM CMOS APS x-ray imager were considered. A discussion of CMOS APS x-ray imager electronic noise sources is provided in Appendix B. σ_{add}^2 can be expressed as the quadratic sum of individual electronic noise elements.

All parameters used in the cascaded system modeling are listed in Table I.

The above analysis assumes that signal and noise conversion gains of CMOS APS are equal. Also, the conversion gain variance is negligible. Therefore, the final output signal can be expressed in electrons referring to photodiode integrated charges. The pixel output signal (d) in e^- is given by $\overline{q_0}$ multiplied by all the gains of all stages,

$$d = a_{pd}^2 \overline{q_0 g_1 g_2 g_4 g_5}. \tag{13}$$

The spatial frequency dependent output signal is the product of d and the system MTF(u,v) given by

$$MTF(u,v) = T_3(u,v) \cdot T_6(u,v). \tag{14}$$

The output noise as a function of spatial frequency can be described by NPS in e^2 mm^2. The NPS can be expressed as follows[27]:

$$NPS(u,v) = a_{pd}^4 \overline{q_0 g_1 g_2 g_4 g_5}\left[1 + \overline{g_4 g_5}(\overline{g_2} + \varepsilon_{g_2})T_3^2(u,v)\right] \times T_6^2(u,v)^{**}III_7(u,v) + S_{add}(u,v), \tag{15}$$

where S_{add} can be calculated by $\sigma_{add}{}^2 \times a_{PIX}{}^2$. The NPS is proportional to the output signal d. In this paper, we describe the NNPS (NNPS in mm^2) by dividing NPS by d^2.

Consecutively, the DQE parameter can be calculated by Eq. (2).

The mean variance of signal (in electrons square) is given by

$$\sigma^2 = \int \int_{u,v=-f_{Nyq}}^{f_{Nyq}} NPS(u,v) \cdot du \cdot dv. \tag{16}$$

The detector SNR (SNR_d) is given by the pixel mean signal divided by its standard deviation,

$$SNR_d = d/\sigma. \tag{17}$$

Unlike the linear PPS imagers, the imaging performance of CMOS APS x-ray imagers at high x-ray exposure levels can be influenced by the signal nonlinearity originated from the varying APS conversion gain. To compensate for the signal nonlinearity, a signal nonlinearity factor f (from 0 to 1) as a function of K_a can be extracted from the derivative of signal response curve.[24] The NNPS is thereby modified to

$$NNPS(u,v) = \frac{\left[1 + \overline{g_4 g_5} f(\overline{g_2} f + \varepsilon_{g_2})T_3^2(u,v)\right]T_6^2(u,v)^{**}III_7(u,v)}{\overline{q_0 g_1 g_2 g_4 g_5} f} + \frac{S_{add}(u,v)}{(a_{pd}^2 \overline{q_0 g_1 g_2 g_4 g_5} f)^2}. \tag{18}$$

In this work, the nonlinearity compensation was applied to both broadband and the monochromatic synchrotron radiations. A more detailed study for the influence of signal and noise nonlinearities on detector performance is presented elsewhere.[45]

2.D. CNR of microcalcifications

It is known that microcalcification detection is critical since it is associated with breast cancer at early stages, which can lead to an interventional procedure.[30] Such early detection is expected to improve the breast cancer detection sensitivity and further reduce the mortality rate. The developed cascaded system model for CMOS APS can be used to evaluate the CNR of microcalcifications for DBT.

In this work, we proposed a simple method based on the Rose model to calculate the CNR of microcalcifications for DBT.[46,47] Specifically, the utility of this method was demonstrated through the calculation of CNR of a two dimensional (2D) projection image in a uniform field for a 1 mm thin slice with microcalcifications. The 1 mm slice width represents the typical focal plane spacing between reconstructed DBT images. The x-ray exposure of a single DBT projection was used in the calculation. It should be noted that 3D image reconstruction is not currently included in our model. However, we believe that the calculated CNR using this simple approach can provide useful information for DBT microcalcification detection without operating a DBT scan and image reconstruction.

To simulate the 3D reconstructed image quality for DBT, additional information of detector performance at various angles, image reconstruction, and ray tracing techniques is needed. This topic is beyond the scope of this paper, but could be an interesting research direction in the future work as an extension of this paper.

The CNR calculation includes both the object contrast information and the detector performance extracted from cascaded system analysis. Based on the Rose model, the CNR can be expressed as[46,47]

$$CNR = \frac{d_b - d_m}{\sigma_b} = C \cdot \frac{d_b}{\sigma_b} = C \cdot SNR_d, \tag{19}$$

where d_b and d_m are the pixel signal for background (breast tissue) and object (microcalcifications), σ_b is the standard deviation of the background signal, and $C = (d_b - d_m)/d_b$ is the contrast of object in surrounding background. SNR_d [Eq. (17)] as a function of K_a was extracted from cascaded system analysis.

The object contrast for microcalcifications can be described by

$$C = 1 - \frac{d_m}{d_b} = 1 - \frac{\int_0^{E_{\max}} \Phi_0(E) \exp\left[-((\mu/\rho)_b \rho_b (t_s - t_m) + (\mu/\rho)_m \rho_m t_m)\right] \cdot \mathrm{d}E}{\int_0^{E_{\max}} \Phi_0(E) \exp\left[-(\mu/\rho)_b \rho_b t_s\right] \cdot \mathrm{d}E}, \quad (20)$$

where $(\mu/\rho)_b$ and $(\mu/\rho)_m$ are the energy-dependent mass attenuation coefficients for breast tissue and microcalcifications,[48] ρ_b (0.93–1.04 g/cm^3 for glandular fraction from 0% to 100%) and ρ_m (~1.54 g/cm^3) are the densities of breast and microcalcifications, t_s is the thickness of the breast slice (~1mm), and t_m is the thickness of microcalcifications. The object contrast and consecutively CNR depend on the material attenuation coefficients and object thickness, but not related to the object area.

Sometimes the image quality is also described by the image SNR (SNR$_i$),[46,47]

$$\mathrm{SNR}_i = \sqrt{n} \cdot \mathrm{CNR}, \quad (21)$$

where n is the number of pixels fully covered by the object. In the optimal case where the object is perfectly aligned with the pixel (i.e., no pixel is partially covered by the object), n can be determined by the number of pixels covered by the object. However, if the object is located in between the pixels (i.e., some of pixels are partially covered), n is effectively reduced. CMOS APS x-ray imagers with a small pixel pitch can achieve a larger n and consecutively SNR$_i$ for a particular object of interest. In this paper, to be consistent with a previous study,[22] CNR instead of SNR$_i$ was used to describe image quality of microcalcifications.

A simulated x-ray spectrum ($\Phi_0(E)$) for a combination of W anode and 0.05 mm Rh filtration (28 kVp) was used.[49,50] Note that $\Phi_0(E)$ considers the incident x-ray spectrum at the breast skin surface, while $\Phi(E)$ as discussed in Sec. 2.C represents the x-ray spectrum at the detector surface attenuated by 1.4 mm external Al filtration.

2.E. MGD for DBT

It is known that current MGD for a single view DBT is similar to that of 2D digital mammography.[4] The MGD calculation for DBT can be considered as an extension of the established 2D method.[51–55] Sechopoulos *et al.* reported the total MGD for a complete DBT scan as[51]

$$\mathrm{MGD} = X \cdot D_g N_0 \cdot \sum_{\alpha} \mathrm{RGD}(\alpha), \quad (22)$$

where X is the breast surface exposure in roentgen (R) per projection, $D_g N_0$ is the normalized glandular dose in mGy/R for the zero degree projection (vertical to the detector), and RGD(α) is the relative glandular dose coefficient at each projection angle α.

The breast surface exposure is calculated from the detector surface air kerma by

$$\frac{X}{K_a} = \frac{\int_0^{E_{\max}} \Phi_0(E) \cdot \xi(E)^{-1} \cdot \mathrm{d}E}{0.008\,76 \times \int_0^{E_{\max}} \Phi_0(E) \cdot \xi(E)^{-1} \cdot \exp\left[-(\mu/\rho)_b \rho_b t_b\right] \cdot \mathrm{d}E}, \quad (23)$$

where $\xi(E)^{-1}$ is the exposure per x-ray fluence,[34] and t_b is the thickness of the compressed breast. The factor 0.00876 was used to convert the x-ray exposure unit from gray to roentgen. Here, we assume that the K_a for each projection is equivalent to the K_a for each slice of DBT image. To simplify the calculation, we fixed the x-ray spectrum $\Phi_0(E)$ for 28 kVp. (In the clinical use, the tube voltage may vary for different breast thicknesses.[4,7])

The normalized glandular dose for mammography and tomosynthesis has been reported for specific x-ray spectra for various anode/filtration combinations.[52–54] Boone reported that the $D_g N_0$ values can be extracted from any arbitrary x-ray spectrum by the following expression[55]:

$$D_g N_0 = \frac{\int_0^{E_{\max}} \Phi_0(E) \cdot \xi(E)^{-1} \cdot D_g N(E) \cdot \mathrm{d}E}{\int_0^{E_{\max}} \Phi_0(E) \cdot \xi(E)^{-1} \cdot \mathrm{d}E}, \quad (24)$$

where $D_g N(E)$ stands for the monoenergetic normalized glandular dose. In this work, $D_g N(E)$ and thus $D_g N_0$ can be calculated using the parameters tabulated by Boone[55]

For our MGD calculation, a DBT scan angle of 15°(±7.5°) and a projection number of 15 were chosen to be consistent with a FDA approved Hologic Selenia Dimensions system.[1,2] At each projection angle α, RGD(α) for a craniocaudal (CC) view was computed using the parameters provided by Sechopoulos *et al.*[51] The MGD for a mediolateral oblique (MLO) view was not evaluated in this work.

3. RESULTS

3.A. Imaging performance of the Dexela 2923 MAM CMOS APS x-ray imager

Figure 3 shows the experimental and fitted data of system MTF for Dexela 2923 MAM CMOS APS x-ray imager. The exponential decay function provides a good fitting to measured system MTF within the Nyquist frequency region (<6.7 lp/mm^{-1}). Data for both HFW and LFW modes were collected using the method described in Sec. 2.A. The detector was tested using both a broadband x-ray radiation with a 150 μm CsI:Tl scintillator and a monochromatic synchrotron radiation with a 200 μm CsI:Tl scintillator.[18,19] The broadband x-ray radiation shows a lower MTF curve compared to the monochromatic synchrotron radiation, even though the CsI:Tl thickness is thinner. Konstantinidis *et al.* demonstrated using monochromatic synchrotron radiation that MTF slightly changes as a function of energy, when the used x-ray energy is below the CsI:Tl K-absorption edge (33.2 keV for I and 36 keV for Cs).[19] The difference in MTF can be related to the variation of broadband and monochromatic synchrotron spectra and different origins of the CsI:Tl scintillators.

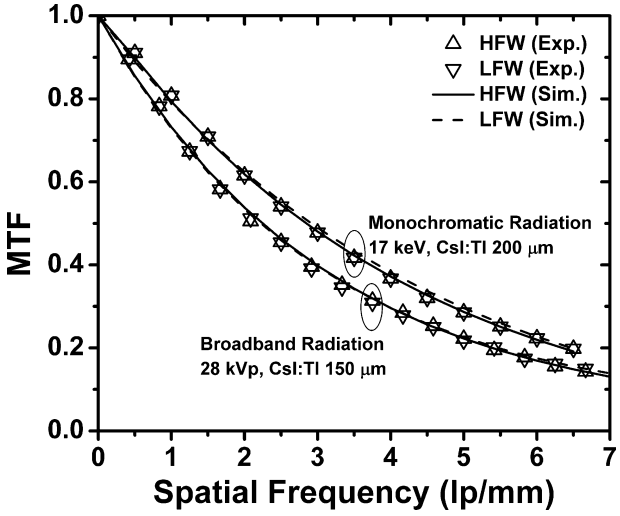

FIG. 3. Measured and fitted MTF for Dexela 2923 MAM CMOS APS x-ray imager using a broadband x-ray radiation with a 150 μm CsI:Tl scintillator and a monochromatic synchrotron radiation with a 200 μm CsI:Tl scintillator. Results for both HFW and LFW modes are shown.

Figures 4 and 5 show the experimental data adopted from Ref. 18 and simulated data of NNPS and DQE parameters for the Dexela 2923 MAM CMOS APS x-ray imager using a clinical broadband x-ray radiation of 28 kVp for HFW and LFW modes, respectively. In both cases, a DQE of greater than 0.7 and ~0.3 can be achieved at a low spatial frequency of

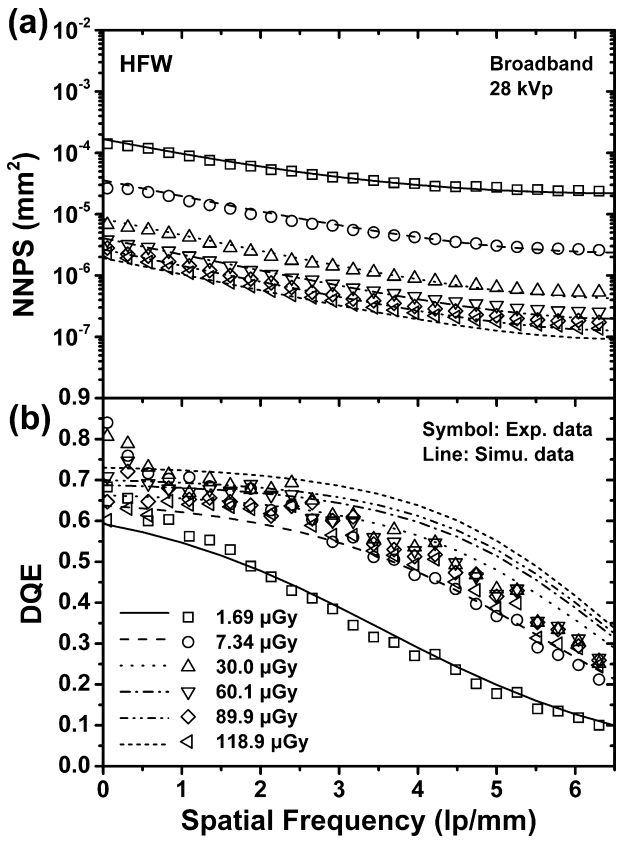

FIG. 4. Experimental (symbols) and simulated (lines) data of NNPS and DQE parameters for the Dexela 2923 MAM CMOS APS x-ray imager (HFW mode) under broadband x-ray radiation of 28 kVp.

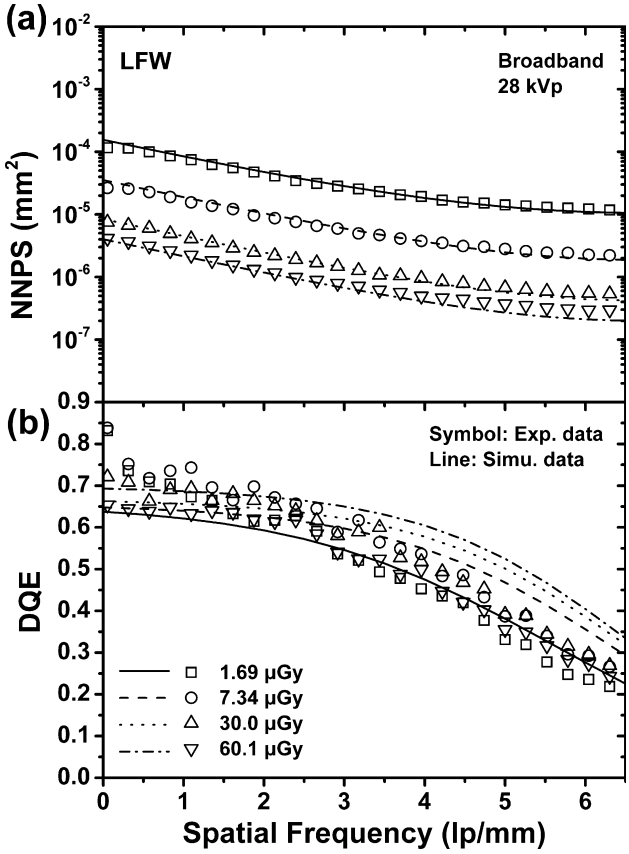

FIG. 5. Experimental (symbols) and simulated (lines) data of NNPS and DQE parameters for the Dexela 2923 MAM CMOS APS x-ray imager (LFW mode) under broadband x-ray radiation of 28 kVp.

0.5 lp/mm [DQE(0.5)] and Nyquist frequency of 6.7 lp/mm [DQE(f_{Nyq})], respectively.

Without signal nonlinearity, the simulated DQE (for both HFW and LFW modes) at zero spatial frequency [DQE(0)] saturates at a value of ~0.65 at $K_a > 60$ μGy, which is lower than the experimental results (>0.7). On the other hand, the simulated DQE with signal nonlinearity fits well the experimental data at low spatial frequencies (<3 lp/mm). The small variation is mainly due to the measurement errors. At the same time, we recognize that there is a deviation of ~19% between experimental and simulated DQEs at spatial frequencies >61 p/mm, which can originate from underestimated electronic noise and neglected FOP blurring stage in the simulation. These deviations have no impact on the analysis presented in this paper.

The K_a for the HFW mode (from 1.69 to 118.9 μGy) covers a wide range; this is possible due to a high full well capacity (1.6×10^6 e$^-$) and a high dynamic range [73 decibels (dB)]. However, at DBT K_a levels (1.69 and 7.34 μGy), the DQE values for HFW mode are low, due to the high electronic noise (360 e$^-$). Even though the dynamic range of LFW mode is lower (69 dB), higher DQE values can be achieved for K_a from 1.69 to 60.1 μGy, which is suitable for DBT application. Therefore, based on this study, we suggest that the LFW mode should be used for a low dose clinical application such as DBT, while the HFW mode is suitable for digital mammography, since it can detect larger signals.

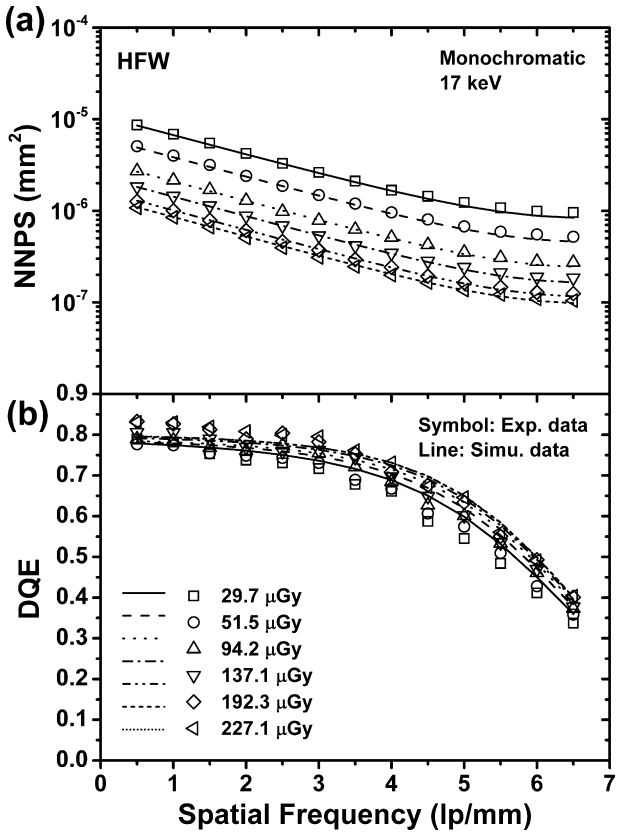

FIG. 6. Experimental (symbols) and simulated (lines) data of NNPS and DQE parameters for the Dexela 2923 MAM CMOS APS x-ray imager (HFW mode) under monochromatic synchrotron radiation of 17 keV.

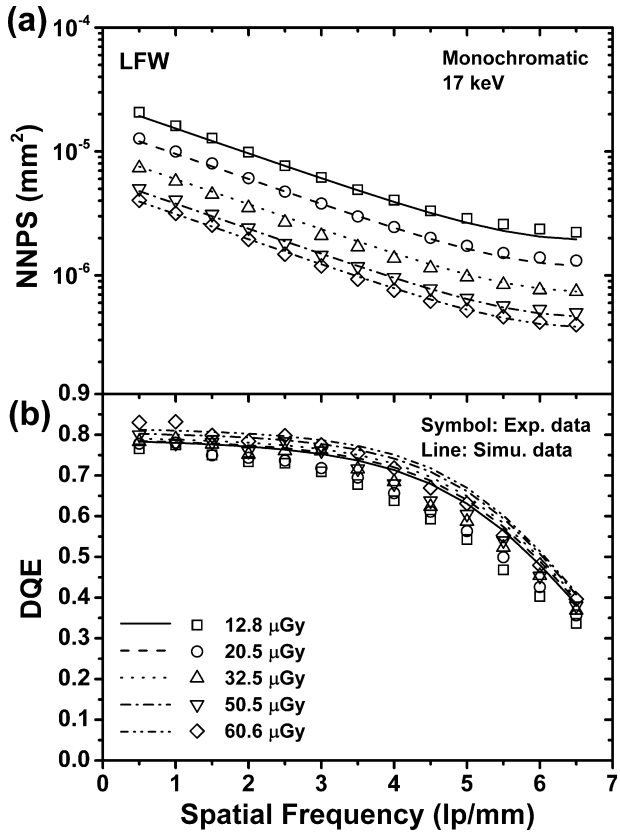

FIG. 7. Experimental (symbols) and simulated (lines) data of NNPS and DQE parameters for the Dexela 2923 MAM x-ray imager (LFW mode) under monochromatic synchrotron radiation of 17 keV.

Figures 6 and 7 show the experimental data adopted from a previous study[19] and simulated data of NNPS and DQE parameters for the Dexela 2923 MAM CMOS APS x-ray imager using monochromatic synchrotron radiation of 17 keV under HFW and LFW modes, respectively. K_a levels from 29.7 to 227.1 μGy and from 12.8 to 60.6 μGy were used for HFW and LFW modes, respectively, which corresponds to digital mammography. The DQE at low frequencies increases as a function of K_a, which indicates existence of signal nonlinearity.

Taking into account the signal nonlinearity, a negligible deviation (around 5%) between simulated and experimental measured DQEs at spatial frequencies <1 lp/mm was achieved. We still observed a deviation of about 10% for at high spatial frequency (>5 lp/mm) region. The results show that DQE(0.5) and DQE(f_{Nyq}) are ~0.8 and ~0.4, respectively.

3.B. CNR of microcalcifications

The extracted SNR_d from the cascaded system analysis can be used to calculate the image quality of microcalcifications described by the CNR [Eq. (19)]. For clinical use, the broadband x-ray radiation of 28 kVp was used and the Dexela 2923 MAM CMOS APS x-ray imager should be operated in the LFW mode. Figure 8 shows the calculated CNR of microcalcifications with diameters of 165, 230, and 400 μm at various MGDs using Eqs. (19), (20), and (22)–(24). The selected microcalcification sizes correspond to a commercial BR3D phantom (CIRS, USA) with a thickness of 5 cm and a glandular fraction of 50%.[22] For x-ray imaging, a minimum CNR of around 3–5 is required to distinguish an object of interest from surrounding background.[4] Park *et al.* reconstructed the microcalcification images [BR3D phantom

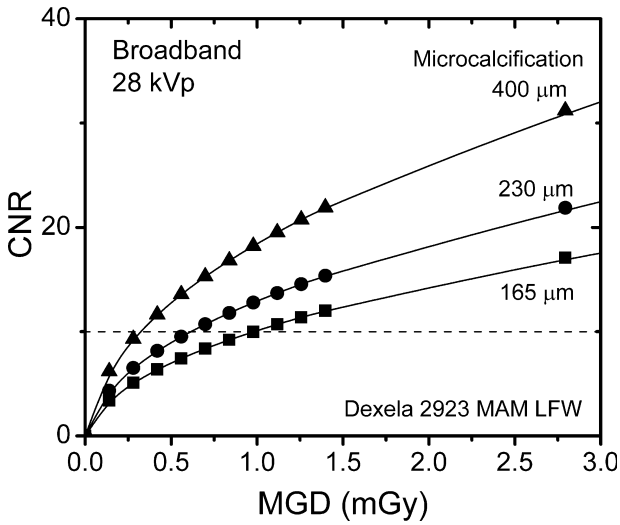

FIG. 8. Calculated CNR of 165, 230, and 400 μm microcalcifications using the Dexela 2923 MAM CMOS APS x-ray imager at MGD up to 3 mGy. A broadband x-ray radiation with tube voltage of 28 kVp was used for this calculation.

(CIRS, USA)] collected using the Dexela 2923 MAM CMOS APS x-ray imager.[22] Their result shows that a CNR of around 10 is sufficient to achieve good image quality of microcalcifications.[22] In current study, a threshold CNR of 10 was also selected. As shown in Fig. 8, the MGDs required to classify microcalcifications of 165, 230, and 400 μm in an average breast (5 cm, 50% glandularity) using the Dexela 2923 MAM CMOS APS x-ray imager are 1.0, 0.6, and 0.3 mGy, respectively.

To distinguish smaller microcalcifications than 165 μm, the aliasing effect needs to be considered. The signal aliasing occurs when the image contains signal power at spatial frequencies higher than the Nyquist frequency determined by the detector pixel pitch ($1/2a_{pix}$).[56,57] Such signal would be mirrored or folded at lower spatial frequencies within the Nyquist frequency limit, causing signal artifacts. Hence, the minimum size of microcalcifications that can be detected without aliasing using the investigated CMOS APS x-ray imager is ~150 μm.[56,57] However, smaller microcalcification detection is desirable, because it can indicate earlier phases of breast cancer and may lead to an immediate interventional procedure.[30] However, to detect microcalcifications with dimensions ranging from 100 to 150 μm, CMOS APS x-ray imager with both a reduced pixel pitch (<50 μm) and a lower electronic noise (<100 e^-) has to be used.[45] The impact of electronic noise on CNR is discussed next.

3.C. Impact of electronic noise on CNR

The main advantage of CMOS APS x-ray imagers is the low electronic noise of, e.g., 165 e^- (Dexela 2923 MAM, LFW mode) in comparison to 1000–2000 e^- for conventional a-Si:H TFT PPS x-ray imagers. The significant electronic noise reduction can lead to improved SNR_d and consecutively CNR. To investigate the impact of electronic noise on CNR, we calculated the CNR by varying σ_{add}.

Figure 9 shows the calculated CNR of 165 μm microcalcifications using the Dexela 2923 MAM CMOS APS x-ray imager at MGD up to 3 mGy (broadband radiation, 28 kVp). Pixel pitches and all other parameters for cascaded system analysis were kept the same. The noise values of 800 and 1500 e^- shown in Fig. 9 correspond to proposed amorphous In–Ga–Zn–O (a-IGZO) TFT APS[58] and indirect a-Si:H PPS x-ray imagers, respectively.[27] The direct a-Se PPS system was not considered in this work. It is shown that CNR decreases for a higher electronic noise at a given MGD value. We can observe that for CNR equal to 10, the required MGDs to distinguish 165 μm microcalcifications are reduced from 2.4 to 1.0 mGy for σ_{add} of 1500 and 165 e^- (Dexela 2923 MAM, LFW mode), respectively. In other words, if the electronic noise is high (>1000 e^-), it is difficult to distinguish small microcalcifications with size of ~165 μm.

The required MGDs to distinguish microcalcifications from 165 to 400 μm using x-ray imagers with various electronic noises are summarized in Fig. 10. It is shown that to classify smaller microcalcifications, a higher MGD is required. It is also observed that the low electronic noise of CMOS APS x-ray imagers can reduce the MGD to below 1 mGy in comparison to detectors with a higher noise (such as a-Se or a-Si:H PPS x-ray imagers).

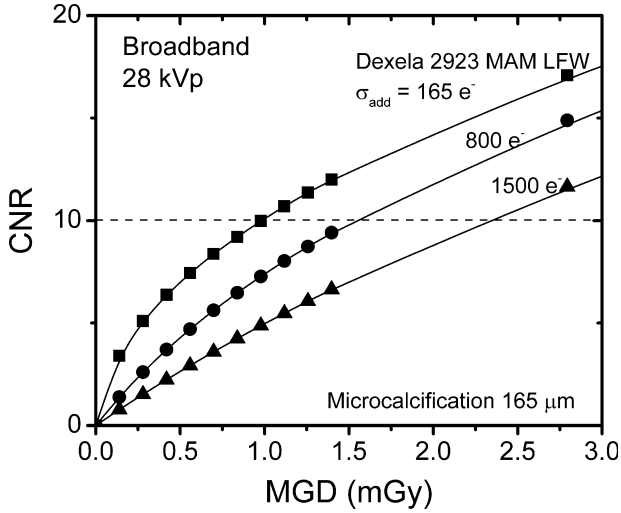

FIG. 9. Calculated CNR of 165 μm microcalcifications using the Dexela 2923 MAM CMOS APS x-ray imager at MGD up to 3 mGy (broadband x-ray radiation, 28 kVp). For comparison purpose, the influence of electronic noise (800–1500 e^-) on CNR is also shown.

Park *et al.* measured the CNR of microcalcifications (165, 230, and 400 μm) from the reconstructed DBT images using the Dexela 2923 MAM CMOS APS x-ray imager at 30 kVp and MGD of 2.0 mGy.[22] Lu *et al.* also extracted the CNR of larger microcalcifications (240, 320, and 540 μm) from the reconstructed images using a General Electric (GE) GEN2 DBT prototype system based on CsI:Tl/a-Si:H PPS (pixel pitch of 100 μm) at 29–33 kVp and MGD of 2.5 mGy.[59] The two sets of experimental CNR data and examples of reconstructed images adopted from Refs. 22 and 59 are shown in Fig. 11. As expected, in comparison to the GE GEN2 a-Si:H based PPS x-ray imager, the CNR values achieved by the Dexela 2923 MAM CMOS APS x-ray imager are higher (by around 10) due to its low electronic noise. By directly

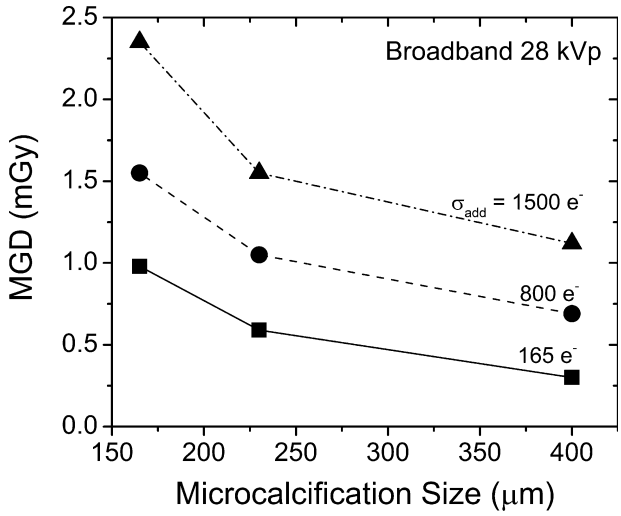

FIG. 10. Required MGD to classify microcalcifications with various sizes using x-ray imagers with different electronic noises. The broadband x-ray radiation of 28 kVp was used in the calculation.

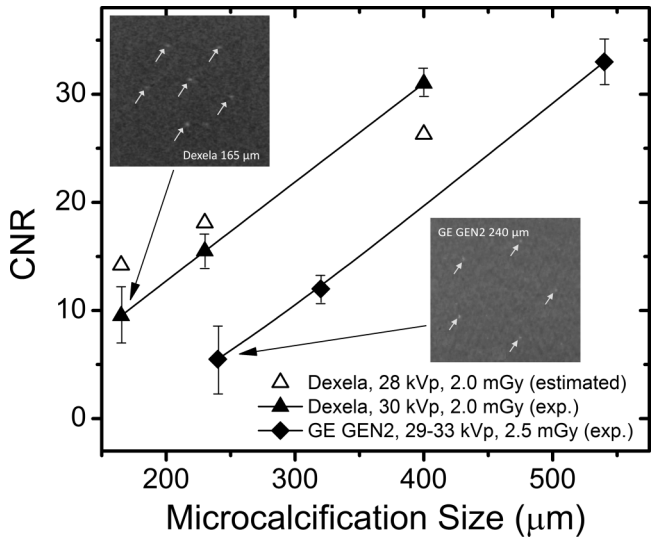

FIG. 11. Estimated CNR using the Dexela 2923 MAM CMOS APS x-ray imager to detect microcalcifications with sizes 165–400 μm at MGD = 2.0 mGy. The CNR of microcalcifications extracted from reconstructed images collected by the Dexela 2923 MAM CMOS APS x-ray imager at MGD = 2.0 mGy (Ref. 22) and a GE GEN2 a-Si:H TFT PPS x-ray imager at MGD = 2.5 mGy (Ref. 59) is shown for comparison purpose.

observing the reconstructed images reported by Park *et al.*[22] and Lu *et al.*,[59] one can tell that 165 μm microcalcifications are still detectable using the Dexela 2923 MAM CMOS APS x-ray imager at MGD of 2.0 mGy, while 240 μm microcalcifications are almost invisible using the GE GEN2 PPS x-ray imager at an even higher MGD of 2.5 mGy. Therefore, smaller microcalcifications can be detected using studied CMOS APS x-ray imager at lower dose. From Fig. 11, we can speculate that it would be very difficult for microcalcifications less than 200 μm to be detected using the conventional a-Si:H based PPS x-ray imager. Using a direct a-Se x-ray imager, Hu and Zhao *et al.* demonstrated that it is possible to improve the visibility of small microcalcifications (<200 μm) by applying a nonuniform dose distribution in combination with a reconstruction slice thickness filter.[60] However, to our best knowledge, the CNR of microcalcifications extracted using the market dominating a-Se based systems is not clearly documented in the literature.

The calculated CNR values based on the proposed model are also shown in Fig. 11. The results are close to the experimental data within experimental errors. The deviation between the calculated and experimental CNR values may originate from the neglected additional noise component generated during image reconstruction and the 2D nature of CNR calculation. However, we believe that the proposed simple model can quickly provide useful information to predict the image quality for DBT without operating a complete DBT testing and image reconstruction.

4. DISCUSSION AND CONCLUSION

A CMOS APS x-ray imager with a 75 μm pixel pitch was characterized and modeled in this work. The Dexela 2923 MAM CMOS APS x-ray imager can operate in both HFW and LFW modes. Based on both experimental data and modeling results, the LFW mode should be used for a low dose application such as DBT due to a large conversion gain of 0.026 DN/e^- and a low electronic noise of 165 e^-. The obtained noise value is much smaller than that of typical direct a-Se and indirect a-Si:H PPS x-ray imagers, which is more than 1000 e^-. Both broadband x-ray radiation and monochromatic synchrotron radiation were evaluated and modeled in this work. The measured DQE value for broadband x-ray radiation is slightly smaller in comparison to a monochromatic synchrotron radiation due to a lower scintillator quantum gain (absorption). For clinical use, a broadband radiation of around 28 kVp should be used. For LFW mode under broadband radiation of 28 kVp, DQE(0.5) and DQE(f_{Nyq}) of more than 0.7 and ~0.3 were achieved.

To evaluate the reconstructed image quality of microcalcifications, we calculated the CNR of microcalcifications with various sizes. It is shown that microcalcifications of 165, 230, and 400 μm in size can be resolved by studied x-ray imager using a MGD of 1.0, 0.6, and 0.3 mGy, respectively. The required MGDs can be reduced to smaller than 1 mGy for an average breast compared to other x-ray imagers (such as a-Si:H based PPS and a-IGZO TFT APS x-ray imagers) having much higher electronic noise values. In comparison to a GE GEN2 prototype DBT x-ray imager (at MGD of 2.5 mGy), the investigated CMOS APS x-ray imager shows an improved CNR and visibility for microcalcifications below 200 μm at a lower MGD (2.0 mGy).

To detect smaller objects ranging from 100 to 150 μm, CMOS APS x-ray imagers with smaller pixel pitch and even lower noise levels must be developed in the near future. Also, impacts of image reconstruction methods on reconstructed image quality should be studied in more detail.

ACKNOWLEDGMENTS

The authors would like to thank Dr. Thalis Anaxagoras (ISDI Ltd., UK) for general discussion related to 3-T CMOS APS imager. We would like to thank Prof. M. M. Goodsitt (University of Michigan) and Dr. A. Badano (FDA) for constructive discussions. One of us (C. Zhao) acknowledges the EECS Department Fellowship (University of Michigan) support.

APPENDIX A: 3-T ACTIVE PIXEL SENSOR OPERATION PRINCIPLE

A typical CMOS APS x-ray imager (e.g., Dexela 2923 MAM) is based on a 3-T pixel circuit in combination with a c-Si PD. The typical c-Si photodiode is simply based on an n^+–p junction. A constant bias V_{DD} is applied to the drain of T_{RST}, while the p-substrate (or p-epitaxial layer) and, thus, the p^--well of the n^+–p junction are grounded.

During the initial reset period [t_{reset} as shown in Fig. 2(b)], the T_{RST} is ON and the imager is in dark ambient. The high voltage V_{DD} is applied to the n^+-well through the inversion channel of the T_{RST} and V_{PD} is reset to V_{DD}. Since the p^--

well is grounded, the n^+–p junction is reversed biased by V_{DD} and a depletion region is formed mainly in the p^--well. The dark current density of the n^+–p diode can be described by a combination of diffusion, thermal generation, and surface recombination current components,[61,62]

$$J_{\text{dark}} \approx \frac{qD_n n_i^2}{L_n N_A} + \frac{qn_i W_D}{\tau_g} + \frac{1}{2} qn_i s_o, \tag{A1}$$

where N_A is the doping concentration of the p^--well, D_n and L_n are the diffusivity and diffusion length for electrons, n_i is the intrinsic carrier density, W_D is the depletion width, τ_g is the generation lifetime, and s_o is the surface recombination rate. The first term represents the diffusion dark current by the minority carriers across the depletion region; the second term is the thermal generation current by the space charge in depletion region; and the third term corresponds to the surface recombination current.

During the integration period, T_{RST} is OFF, while the x-ray source is ON. As shown in Fig. 2(b), pulsed x-ray source is used with integration time of t_{int} (~10 ms for DBT). As discussed in Sec. 2, the x-rays generate optical photons in the scintillator. The impinging photons generate e–h pairs inside the photodiode depletion region which are separated into carriers by the electric field. Then, electrons are collected by the n^+-well, while the holes are removed from p^--well through p-substrate to GND. The stored charge in the n^+-well decreases the potential V_{PD} below V_{DD}. The potential of n^+-well V_{PD} is given by

$$V_{PD} = V_{DD} - \frac{J_{\text{photo}} A_{PD} t_{\text{int}}}{C_{PD}}, \tag{A2}$$

where J_{photo} is the photocurrent density; A_{PD} is the area of photodiode ($75 \times 75 \times 0.84$ μm^2 for Dexela MAM x-ray imager); C_{PD} is the pixel capacitance (estimated to be in the range of 27–81 fF), which can be described by the product of c-Si permittivity and A_{PD} divided by depletion width of photodiode p–n junction; and t_{int} is the integration time.

If we neglect the dark current terms, the photocurrent of c-Si photodiode is given by[63]

$$J_{\text{photo}} = q \cdot \frac{\Phi_4 \cdot (1-R)}{h\nu_m} \left[1 - \frac{\exp(-\alpha W_D)}{1+\alpha L_n} \right], \tag{A3}$$

where α is the absorption coefficient (in cm^{-1}) of c-Si, W_D is the deletion width of n^+–p junction, R is the total reflectance of the FOP/SiO_2 interface and SiO_2/Si interface, $h\nu_m$ is the mean photon energy of the optical emission spectrum, and Φ_4 is the mean incident light intensity. Example of the driving schemes of the reset and integration stages is shown in Fig. 2(b).

The parameter EQE determines the ratio of the number of collected carriers by photodiode to the number of the incident photons, which is given by[63]

$$\text{EQE} = \frac{h\nu_m}{q} \cdot \frac{J_{\text{photo}}}{\Phi_4} = (1-R) \left[1 - \frac{\exp(-\alpha W_D)}{1+\alpha L_n} \right]. \tag{A4}$$

To achieve a large EQE, the total reflectance R has to be minimized, and the product of αW_D needs to be maximized.

After the reset and integration stages, the signal (V_{PD}) is readout through T_{SF} and T_{SEL} to the readout electronics. During readout period, both T_{SEL} and the column bias transistor T_{BIAS} are turned ON. The readout time is t_{read} as shown in Fig. 2(b). The readout electronics can be simplified to a column storage capacitor (C_{COL}) and an operational amplifier (op-amp).[61,64] The output current following through T_{SF} and T_{SEL} charges up the column storage capacitor C_{COL}. The voltage on the column storage capacitor (V_{COL}) is amplified and read as the output voltage V_{OUT}. T_{BIAS} is biased such that it works in the saturation region and its drain-to-source current I_{BIAS} is given by

$$I_{BIAS} = \frac{1}{2} \left(\frac{W}{L} \right)_{BIAS} \mu_n C_{ox} (V_{G,BIAS} - V_{T,BIAS})^2, \tag{A5}$$

where $(W/L)_{BIAS}$ is the channel width over length T_{BIAS}, μ_n is the electron mobility, C_{ox} is the oxide capacitance per unit area, $V_{G,BIAS}$ is the gate voltage, and $V_{T,BIAS}$ is the threshold voltage of T_{BIAS}.

Neglecting the on-resistance of T_{SEL}, the output current of APS pixel I_{OUT} is determined by the gate-to-source voltage of T_{SF}. Since T_{SF} is operating in saturation region ($V_{DD} > V_{PD} - V_{T,RST}$), the total pixel output current can be expressed as[64]

$$I_{BIAS} + C_{COL} \frac{dV_{COL}}{dt} = \frac{K_{SF}}{2} (V_{PD} - V_{T,SF} - V_{COL})^2, \tag{A6}$$

where $V_{T,SF}$ is the threshold voltage of T_{SF}, and K_{SF} is given by

$$K_{SF} = \left(\frac{W}{L} \right)_{SF} \mu_n C_{ox}, \tag{A7}$$

where $(W/L)_{COL}$ is the transistor channel width over length of T_{SF}. V_{COL} as a function of readout time t is given by[62]

$$V_{COL}(t) = V_{PD} - V_{T,SF} - \beta \left(\frac{1 + \frac{\alpha-\beta}{\alpha+\beta} \exp\left(-\frac{\beta K_{SF}}{C_{COL}} t\right)}{1 - \frac{\alpha-\beta}{\alpha+\beta} \exp\left(-\frac{\beta K_{SF}}{C_{COL}} t\right)} \right), \tag{A8}$$

where $\alpha = V_{PD} - V_{T,SF} - V_{COL}(0)$ and $\beta = \sqrt{2I_{BIAS}/K_{SF}}$. For sufficient long readout time, V_{COL} is saturated and the CMOS APS output voltage V_{OUT} is given by

$$V_{OUT} = \gamma V_{COL}(\infty) = \gamma (V_{PD} - V_{T,SF} - \beta), \tag{A9}$$

where γ is the voltage gain of the op-amp given by V_{OUT}/V_{COL}.

The conversion gain (in volts/electron) of the APS pixel and readout electronics is given by the derivative of V_{OUT} to the total number of input charges (Q_{IN}/q),

$$G = \frac{\partial V_{OUT}}{\partial Q_{IN}/q} = \frac{\gamma q}{C_{PD}} \frac{\partial V_{OUT}}{\partial V_{PD}} = \frac{\gamma q}{C_{PD}}. \tag{A10}$$

Assuming that γ is ~10 and C_{PD} is from 27 to 81 fF, the estimated conversion gain G is in the range of 20–59 $\mu V/e^-$. It may be observed that the conversion gain is inversely proportional to the capacitance of photodiode. In the ideal case, the conversion gain is not dependent on semiconductor carrier mobility using the readout electronics as shown in Fig. 2. Therefore, to achieve a large conversion gain, the photodiode capacitance needs to be reduced. But when we reduce C_{PD}, the number of collected carrier is also reduced. Hence, we need to reach a compromise between C_{PD} and photodiode area. In reality, C_{PD} is not a constant but dependent on V_{PD}. Therefore, G is also a function of V_{PD}, which will result in signal nonlinearity.

Finally, an analog-to-digital converter (ADC) is used to convert the signal in volts to a DN. It should be noticed that

in modern CMOS APS x-ray imager such as the Dexela 2923 MAM, the real signal is obtained by subtracting the average dark signal over a number (e.g., Ref. 32) of dark frames.

APPENDIX B: ELECTRONIC NOISE OF 3-T APS

We consider that the pixel electronic noise of 3-T CMOS APS x-ray imager consists of the photodiode dark current shot noise, reset (kTC) noise of T_{RST}, thermal and flicker ($1/f$) noise of T_{SF}, T_{SEL}, and T_{BIAS}, and dark fixed pattern noise (FPN).[65–67] Other sources of noise such as op-amp and ADC noise can also contribute to the total read noise. However, it is very difficult to quantify the op-amp noise. We are mainly interested in the input-referred noise (referred to the input sensing node, V_{PD} as in Fig. 2) in electrons for the cascaded system analysis operated in this paper.

The input referred photodiode dark current shot noise in e^- is given by

$$\sigma_{dark} = \sqrt{J_{dark} A_{PD} t_{frame}/q}, \tag{B1}$$

where J_{dark} (~10 pA/cm^2) is the dark current density of photodiode, A_{PD} (75×75 μm$^2\times0.84$) is the photodiode area, and t_{frame} (~200 ms for DBT considering a readout speed of 5 fps) is the frame time. The calculated σ_{dark} is ~24 e^-, which is very small, thanks to a low dark current of photodiode.

The input referred reset kTC noise in e^- is given by

$$\sigma_{reset} = \sqrt{kTC_{PD}}/q. \tag{B2}$$

For estimated C_{PD} ranging from 27 to 81 fF for LFW mode, the calculated σ_{reset} is in the range of 66–114 e^-. For HFW mode, the C_{PD} in Eq. (B2) is replaced by the total input capacitance ($C_S + C_{PD}$) ranging from 85 to 255 fF. The calculated σ_{reset} for HFW mode is in the range of 117–203 e^-.

The output-referred thermal noise (referred to V_{COL}) in μV of T_{SF}, T_{SEL}, and T_{COL} without considering the op-amp gain (γ) has been discussed in detail by Tian *et al.*[65] The input-referred thermal noise in e^- of T_{SF} ($\sigma_{th,SF}$), T_{SEL} ($\sigma_{th,SEL}$), and T_{BIAS} ($\sigma_{th,COL}$) can be derived by multiplying the thermal noise by a factor of γ/G,

$$\sigma_{th,SF} = \frac{\gamma}{G}\sqrt{\frac{2}{3}\frac{kT}{C_S}\frac{1}{1+g_{m,SF}/g_{d,SEL}}}, \tag{B3}$$

$$\sigma_{th,SEL} = \frac{\gamma}{G}\sqrt{\frac{kT}{C_S}\frac{1}{g_{d,SEL}\left(\frac{1}{g_{d,SEL}}+\frac{1}{g_{m,SF}}\right)}}, \tag{B4}$$

$$\sigma_{th,BIAS} = \frac{\gamma}{G}\sqrt{\frac{2}{3}\frac{kT}{C_S}g_{m,BIAS}\left(\frac{1}{g_{d,SEL}}+\frac{1}{g_{m,SF}}\right)}, \tag{B5}$$

where $g_{m,SF}$, $g_{d,SEL}$, and $g_{m,BIAS}$ represent the transconductance of T_{SF}, channel conductance of T_{SEL}, and transconductance of T_{BIAS}, respectively. For CMOS APS, the input-referred thermal noise is minimized by G/γ on the order of 1 μV/e^-. Also based on our calculation in Ref. 45, the flicker noise (σ_{fl}) of transistors (around 20 e^-) can also be reduced by G/γ and will not be a dominant noise source.

The spatial nonuniformity of CMOS APS array results in the time-independent FPN both in dark (also known as the offset FPN) and under illumination.[66,67] One source of offset FPN is originated from the pixel-to-pixel transistor parameter (such as threshold voltage) mismatch. Another source of FPN is the photodiode dark current variation over large area, which is commonly referred to as dark signal nonuniformity (σ_{DSNU}).[3,38] The FPN under illumination is also called gain FPN or photoresponse nonuniformity (σ_{PRNU}), which is originated from the conversion gain mismatch of different pixels.[10,62] Gain FPN is proportional to integration time and depends on the dark FPN (as the offset of FPN under illumination).[62] During the NPS measurements described in this paper, the FPN was removed using a gain and offset correction algorithm without introducing propagated uncorrelated noise to the corrected flat images.[68]

The total electronic noise can be given by

$$\sigma_{add}^2 = \sigma_{dark}^2 + \sigma_{reset}^2 + \sigma_{th}^2 + \sigma_{fl}^2 + \sigma_{DSNU}^2 + \sigma_{PRNU}^2. \tag{B6}$$

The measured σ_{add} for Dexela 2923 MAM CMOS APS x-ray imager is 360 and 165 e^- for HFW and LFW modes, respectively, which is greater than calculated σ_{add} (119–204 e^- for HFW mode and 70–116 e^- for LFW). The difference between the measured and estimated noise values may come from the sources of thermal noise, flicker noise, FPN, op-amp noise, and ADC noise neglected in the calculation.

To realize even better CMOS APS x-ray imager for DBT with reduced noise value and higher resolution, we suggest that a 4-T CMOS APS x-ray imager with a pinned photodiode (PPD) and CDS readout electronics should be considered in the near future.[10,69–71] The PPD will be used to suppress the dark current and kTC noise, while the CDS technology can be used to minimize the FPN. However, to realize such new x-ray imagers, an extended x-ray source should be used, which will probably generate additional dose for the patient. Further studies are needed to see if such novel x-ray source in combination with 4-T CMOS APS technology implementation is possible.

[a]Author to whom correspondence should be addressed. Electronic mail: kanicki@eecs.umich.edu

[1]J. A. Baker and J. Y. Lo, "Breast tomosynthesis: State-of-the-art and review of the literature," Acad. Radiol. **18**, 1298–1310 (2011).
[2]I. Sechopoulos, "A review of breast tomosynthesis. Part I. The image acquisition process," Med. Phys. **40**, 014301 (12pp.) (2013).
[3]C. Ghetti, A. Borrini, O. Ortenzia, R. Rossi, and P. L. Ordonez, "Physical characteristics of GE senographe essential and DS digital mammography detectors," Med. Phys. **35**, 456–463 (2008).
[4]Technical evaluation of Hologic Selenia Dimensions digital breast tomosynthesis system, NHSBSP equipment report 1307, available at http://www.cancerscreening.nhs.uk/breastscreen/publications/nhsbsp-equipment-report-1307.pdf.
[5]B. Zhao and W. Zhao, "Imaging performance of an amorphous selenium digital mammography detector in a breast tomosynthesis system," Med. Phys. **35**, 1978–1987 (2008).
[6]R. L. Weisfield and N. R. Bennett, "Electronic noise analysis of a 127 μm pixel TFT/photodiode array," Proc. SPIE **4320**, 209–218 (2001).
[7]S. S. J. Feng and I. Sechopoulos, "Clinical digital breast tomosynthesis system: Domestic characterization," Radiology **263**, 35–42 (2012).
[8]E. R. Fossum, R. H. Nixon, and D. Schick, "A 37×28 mm^2 600 k-pixel CMOS APS dental x-ray camera-on-a-chip with self-triggered readout,"

in *IEEE International Solid-State Circuits Conference. Digest of Technical Papers* (IEEE, San Francisco, CA, 1998), pp. 172–173.
[9]H. K. Kim, G. Cho, S. W. Lee, Y. H. Shin, and H. S. Cho, "Development and evaluation of a digital radiographic system based on CMOS image sensor," IEEE Trans. Electron Devices **48**, 662–666 (2001).
[10]A. El Gamal and H. Eltoukhy, "CMOS image sensors," IEEE Circuits Devices Mag. **21**, 6–20 (2005).
[11]E. R. Fossum and D. B. Hondongwa, "A review of the pinned photodiode for CCD and CMOS image sensors," IEEE J. Electron. Device Soc. **2**, 33–43 (2014).
[12]C. D. Arvanitis, S. E. Bohndiek, G. Royle, A. Blue, H. X. Liang, A. Clark, M. Prydderch, R. Turchetta, and R. Speller, "Empirical electro-optical and x-ray performance evaluation of CMOS active pixels sensor for low dose, high resolution x-ray imaging," Med. Phys. **34**, 4612–4625 (2007).
[13]M. Esposito, T. Anaxagoras, A. Fant, K. Wells, A. Konstantinidis, J. P. F. Osmond, P. M. Evans, R. D. Speller, and N. M. Allinson, "DynAMITe: A wafer scale sensor for biomedical applications," J. Instrum. **6**, C12064 (2011).
[14]M. Farrier, T. G. Achterkirchen, G. P. Weckler, and A. Mrozack, "Very large area CMOS active-pixel sensor for digital radiography," IEEE Trans. Electron Devices **56**, 2623–2631 (2009).
[15]S. E. Bohndiek, A. Blue, J. Cabello, A. T. Clark, N. Guerrini, P. M. Evans, E. J. Harris, A. Konstantinidis, D. Maneuski, J. Osmond, V. O'Shea, R. D. Speller, R. Turchetta, K. Wells, H. Zin, and N. M. Allinson, "Characterization and testing of LAS: A prototype 'large area sensor' with performance characteristics suitable for medical imaging applications," IEEE Trans. Nucl. Sci. **56**, 2938–2946 (2009).
[16]A. C. Konstantinidis, M. B. Szafraniec, R. D. Speller, and A. Olivo, "The Dexela 2923 CMOS x-ray detector: A flat panel detector based on CMOS active pixel sensors for medical imaging applications," Nucl. Instrum. Methods Phys. Res., Sect. A **689**, 12–21 (2012).
[17]M. Esposito, T. Anaxagoras, A. C. Konstantinidis, Y. Zheng, R. D. Speller, P. M. Evans, N. M. Allinson, and K. Wells, "Performance of a novel wafer scale CMOS active pixel sensors for bio-medical imaging," Phys. Med. Biol. **59**, 3533–3554 (2014).
[18]T. Patel, K. Klanian, Z. Gong, and M. B. Williams, "Detective quantum efficiency of CsI-CMOS x-ray detector for digital breast tomosynthesis operating in high dynamic range and high sensitivity modes," Breast Imaging **7361**, 80–87 (2012).
[19]A. C. Konstantinidis, M. B. Szafraniec, L. Rigon, G. Tromba, D. Dreossi, N. Sodini, P. F. Liaparinos, S. Naday, S. Gunn, A. Mcarthur, R. D. Speller, and A. Olivo, "X-ray performance evaluation of the Dexela CMOS APS x-ray detector using monochromatic synchrotron radiation in the mammographic energy range," IEEE Trans. Nucl. Sci. **60**, 3969–3980 (2013).
[20]S. Naday, E. Bullard, S. Gunn, J. Brodrick, E. O'Tuairisg, A. McArthur, H. Amin, M. Williams, P. Judy, and A. Konstantinidis, "Optimised breast tomosynthesis with a novel CMOS flat panel detector," in *Proceedings of the 10th International Workshop on Digital Mammography* (Springer, Berlin, Heidelberg, Girona, Spain, 2010), pp. 428–435.
[21]Y. Kim, H. Kim, H. Park, J. Choi, and Y. Choi, "Clinical performance evaluation of the prototype digital breast tomosynthesis system," Proc. SPIE **8313**, 83134R (2012).
[22]H. S. Park, Y. S. Kim, H. J. Kim, Y. W. Choi, and J. G. Choi, "Optimization of configuration parameters in a newly developed digital breast tomosynthesis system," J. Radiat. Res. **55**, 589–599 (2014).
[23]S. Vedantham, A. Karellas, and S. Suryanarayanan, "Solid-state fluoroscopic imager for high-resolution angiography: Parallel-cascaded linear system analysis," Med. Phys. **31**, 1258–1268 (2004).
[24]J. H. Siewerdsen, L. E. Antonuk, Y. El-Mohri, J. Yorkston, W. Huang, and J. M. Boudry, "Empirical and theoretical investigation of the noise performance of indirect detection, active matrix flat-panel imagers (AMFPIs) for diagnostic radiology," Med. Phys. **24**, 71–89 (1997).
[25]I. A. Cunningham, M. S. Westmore, and A. Fenster, "A spatial-frequency dependent quantum accounting diagram and detective quantum efficiency model of signal to noise propagation in cascaded imaging systems," Med. Phys. **21**, 417–427 (1994).
[26]J. H. Siewerdsen, L. E. Antonuk, Y. El-Mohri, J. Yorkston, W. Huang, and I. A. Cunningham, "Signal, noise power spectrum, and detective quantum efficiency of indirect-detection flat-panel imagers for diagnostic radiology," Med. Phys. **25**, 614–628 (1998).
[27]Y. El-Mohri, L. E. Antonuk, Q. Zhao, Y. Wang, Y. Li, H. Du, and A. Sawant, "Performance of a high fill factor, indirect detection prototype flat-panel imager for mammography," Med. Phys. **34**, 315–327 (2007).
[28]D. J. Tward and J. H. Siewerdsen, "Cascaded systems analysis of the 3D noise transfer characteristics of flat-panel cone-beam CT," Med. Phys. **35**, 5510–5529 (2008).
[29]B. Zhao and W. Zhao, "Three-dimensional linear system analysis for breast tomosynthesis," Med. Phys. **35**, 5219–5232 (2008).
[30]F. W. Wheeler, A. G. Amitha perera, B. E. Claus, S. L. Muller, G. Peters, and J. P. Kaufhold, "Micro-calcification detection in digital tomosynthesis mammography," Proc. SPIE **6144**, 614420 (2006).
[31]International Electrotechnical Commission, Medical electrical equipment—Characteristics of digital x-ray imaging devices—Part 1-2: Determination of the detective quantum efficiency—Detector used in mammography, IEC 62220-1-2, IEC, Gerneva, 2007.
[32]E. Buhr, S. Günther-Kohfahl, and U. Neitzel, "Accuracy of a simple method for deriving the presampled modulation transfer function of a digital radiographic system from an edge image," Med. Phys. **30**, 2323–2331 (2003).
[33]E. Samei, M. J. Flynn, and D. A. Reimann, "A method for measuring the presampled MTF of digital radiographic system suing an edge test device," Med. Phys. **25**, 102–113 (1998).
[34]J. M. Boone, "X-ray production interaction and detection in diagnostic imaging," in *Handbook of Medical Imaging Physics and Psychophysics* (SPIE, Bellingham, WA, 2000), Chap. 1, pp. 37–67.
[35]M. J. Yaffe and J. A. Rowlands, "X-ray detectors for digital radiography," Phys. Med. Biol. **42**, 1455–1466 (1997).
[36]J. G. Rocha and S. Lanceros-Mendez, "Review on x-ray detectors based on scintillators and CMOS technology," Recent Pat. Electr. Eng. **4**, 16–41 (2011).
[37]W. Zhao, G. Ristic, and J. A. Rowlands, "X-ray imaging performance of structured cesium iodide scintillators," Med. Phys. **31**, 2594–2605 (2004).
[38]P. A. Rodnyi, P. Dorenbos, and C. W. E. Van Eijk, "Energy loss in inorganic scintillators," Phys. Status Solidi B **187**, 15–29 (1995).
[39]M. Nikl, "Scintillation detectors for x-rays," Meas. Sci. Technol. **17**, R37–R54 (2006).
[40]R. C. Ronda, in *Luminescence: From Theory to Applications* (John Wiley & Sons, Inc., New York, NY, 2007), Chap. 1, pp. 1–34.
[41]I. Holl, E. Lorenz, and G. Mageras, "A measurement of light yield of common inorganic scintillators," IEEE Trans. Nucl. Sci. **35**, 105–109 (1988).
[42]W. Hillen, W. Eckenbach, Q. Quadflieg, and T. Zaengel, "Signal-to-noise performance in cesium iodide x-ray fluorescent screens," Proc. SPIE **1443**, 120–131 (1991).
[43]FOS (fiber optic plate with scintillator) for digital x-ray imaging, Technical Information, Hamamatsu, 1996.
[44]S. Hejazi and D. P. Trauernicht, "System considerations in CCD-based x-ray imaging for digital chest radiography and digital mammography," Med. Phys. **24**, 287–297 (1997).
[45]C. Zhao, A. C. Konstantinidis, Y. Zheng, T. Anaxagoras, R. D. Speller, and J. Kanicki, "50 μm pixel pitch wafer-scale CMOS x-ray detector for digital breast tomosynthesis: Characterization and nonlinear cascaded system analysis," Phys. Med. Biol. (in press, Nov. 2015 issue).
[46]W. Zhao, R. Deych, and E. Dolazza, "Optimization of operational conditions for direct digital mammography detectors for digital breast tomosynthesis," Proc. SPIE **5745**, 1272–1281 (2005).
[47]A. E. Burgess, "The Rose model revisited," J. Opt. Soc. Am. A **16**, 633–646 (1999).
[48]J. H. Hubbel and S. M. Seltzer, "Tables of x-ray mass attenuation coefficient and mass energy-absorption coefficients 1 keV to 20 MeV for elements Z = 1 to 92 and 48 additional substances of dosimetric interest," Report No. NISTIR 5632 (NIST, Gaithersburg, MD, 1995).
[49]J. M. Boone and A. Seibert, "An accurate method for computer-generating tungsten anode x-ray spectra from 30 to 140 kV," Med. Phys. **24**, 1661–1670 (1997).
[50]J. M. Boone, "Spectral modeling and compilation of quantum fluence in radiography and mammography," Proc. SPIE **3336**, 592–601 (1998).
[51]I. Sechopoulos, S. Suryanarayanan, S. Vedantham, C. D'Orsi, and A. Karellas, "Computation of the glandular radiation dose in digital tomosynthesis of the breast," Med. Phys. **34**, 221–232 (2007).
[52]D. R. Dance, "Monte Carlo calculation of conversion factors for the estimation of mean glandular breast dose," Phys. Med. Biol. **35**, 1211–1219 (1990).
[53]D. R. Dance, C. L. Skinner, K. C. Young, J. R. Beckett, and C. J. Kotre, "Additional factors for the estimation of mean glandular breast dose us-

ing the UK mammography dosimetry protocol," Phys. Med. Biol. **34**, 3225–3240 (2000).
[54]X. Wu, G. T. Barnes, and D. M. Tucker, "Normalized average glandular dose in molybdenum target-rhodium filter and rhodium target-rhodium filter mammography," Radiology **193**, 83–89 (1994).
[55]J. M. Boone, "Normalized glandular dose (DgN) coefficients for arbitrary x-ray spectra in mammography: Computer-fit values of Monte Carlo derived data," Med. Phys. **29**, 869–875 (2002).
[56]J. A. Rowlands, W. G. Ji, W. Zhao, and D. L. Lee, "Direct conversion flat panel x-ray imaging: Reduction of noise by presampling filtration," Proc. SPIE **3977**, 447–456 (2000).
[57]E. Samei, "Performance of digital radiography detectors: Factors affecting sharpness and noise," in *Advances in Digital Radiography* (Radiological Society of North America (RSNA), Oak Brook, IL, 2003), pp. 49–61.
[58]C. Zhao and J. Kanicki, "Amorphous In–Ga–Zn–O thin-film transistor active pixel sensor x-ray imager for digital breast tomosynthesis," Med. Phys. **41**, 091902 (14pp.) (2014).
[59]Y. Lu, H.-P. Chan, J. Wei, M. Goodsitt, P. L. Carson, L. Hadjiishi, A. Schmitz, J. W. Eberhard, and B. E. H. Claus, "Image quality of microcalcifications in digital breast tomosynthesis: Effects of projection view distributions," Med. Phys. **38**, 5703–5712 (2011).
[60]Y.-H. Hu and W. Zhao, "The effect of angular dose distribution on the detection of microcalcifications in digital breast tomosynthesis," Med. Phys. **38**, 2455–2466 (2011).
[61]J. Ohta, in *Smart CMOS Image Sensors and Applications* (CRC, Boca Raton, FL, 2010), Chap. 2, pp. 12–57.
[62]X. Wang, "Noise in sub-micron CMOS image sensors," Master thesis (University of Southampton, Southampton, UK, 2008), Chap. 2, pp. 13–41; Chap. 3, pp. 45–71.
[63]S. M. Sze and K. K. Ng, "Photodetectors and solar cells," in *Physics of Semiconductor Devices* (John Wiley & Sons, Inc., New York, NY, 2007), Chap. 13, pp. 663–742.
[64]K. Salama and A. El Gamal, "Analysis of active pixel sensor readout circuit," IEEE Trans. Circuits Syst., I: Fundam. Theory Appl. **50**, 941–945 (2003).
[65]H. Tian, B. Fowler, and A. El Gamel, "Analysis of temporal noise in CMOS photodiode active pixel sensor," IEEE J. Solid-State Circuits **36**, 92–101 (2001).
[66]R. H. Nixon, S. E. Kemeny, B. Pain, C. O. Staller, and E. R. Fossum, "256 × 256 CMOS active pixel sensor camera-on-a-chip," IEEE J. Solid-State Circuits **31**, 2046–2050 (1996).
[67]M. Bigas, E. Cabruja, J. Forest, and J. Salvi, "Review of CMOS image sensors," Microelectron. J. **37**, 433–451 (2006).
[68]A. C. Konstantinidis, A. Olivo, and R. D. Speller, "Technical note: Modification of the standard gain correction algorithm to compensate for the number of used reference flat frames in detector performance studies," Med. Phys. **38**, 6683–6687 (2011).
[69]B. C. Burkey, W. C. Chang, J. Littlehale, T. H. Lee, T. J. Tredwell, J. P. Lavine, and E. A. Trabka, "The pinned photodiode for an interline-transfer CCD image sensor," in *Proceedings of International Electron Devices Meeting* (IEEE, San Francisco, CA, 1984), pp. 28–31.
[70]R. M. Guidash, T. H. Lee, P. P. K. Lee, D. H. Sackett, C. I. Drowley, M. S. Swensen, L. Arbaugh, R. Hollstein, F. Shapiro, and S. Domer, "A 0.6 μm CMOS pinned photodiode color imager technology," in *Proceedings of International Electron Devices Meeting* (IEEE, Washington, DC, 1997), pp. 927–929.
[71]T. Lulé, S. Benthien, H. Keller, F. Mütze, P. Rieve, K. Seibel, M. Sommer, and M. Böhm, "Sensitivity of CMOS based imagers and scaling perspectives," IEEE Trans. Electron Devices **47**, 2110–2122 (2000).